Single atom catalysts for triiodide adsorption and fast conversion to boost the performance of aqueous zinc−iodine batteries†

Fuhua Yang, [ID] ‡[ab] Jun Long,‡[c] Jodie A. Yuwono,‡[a] Huifang Fei,[b] Yameng Fan,[d] Peng Li,[e] Jinshuo Zou,[a] Junnan Hao, [ID] [a] Sailin Liu,[a] Gemeng Liang,[a] Yanqiu Lyu, [ID] [a] Xiaobo Zheng,[f] Shiyong Zhao,*[a] Kenneth Davey [ID] [a] and Zaiping Guo [ID] *[a]

Zinc−iodine (Zn−I_2) batteries are promising for energy storage because of their low cost, environmental friendliness, and attractive energy density. However, triiodide dissolution and poor conversion kinetics hinder their application. Herein, we demonstrated that the 'shuttle effect' in Zn−I_2 batteries can be suppressed *via* single atom catalyst (SAC) cathodes because of efficient catalytic activity in I_2/I_3^-/I^- reactions and their ability to adsorb I_3^-. Based on DFT computations, an I^- poisoning mechanism was proposed for SAC selection to suppress the shuttle effect in Zn−I_2 batteries. I^- formation and desorption are crucial to maintaining the catalytic and adsorption role of metallic elements. SACu favours the reduction of I_2 to I and exhibits a low energy barrier to release I^- from the surface, thus allowing more rapid conversion kinetics, while at the same time suppressing the shuttle effect of I_3^- in Zn−I_2 batteries. In contrast, without sufficient energy, the final product of I^- will remain adsorbed at the metal site of SAFe, SAMn, SAV, and SATi, thus killing the catalytic activity of SACs to facilitate the iodine reduction reaction (IRR). To confirm practicality, single-atom Cu-embedded nitrogen-doped Ketjen black (SACu@NKB), together with SACo@NKB and NKB, were synthesized and electrochemically assessed. The as-prepared SACu@NKB outperformed the SACo@NKB and NKB cathodes in terms of reversible capacity and cycle life. In addition, a rate-limiting step in these redox reactions was identified, and overpotential was estimated, and these were found to be dependent on the d-band centre of SACs. A lower d-band centre can be associated with more optimal catalytic performance in SACs. This work reveals that the superior cycle life of Zn−I_2 batteries is underpinned by the catalytic and adsorption role of metallic catalysts, and we report an in-depth understanding of how this boosts the performance of Zn−I_2 batteries, with implications for future long-life battery design.

Broader context

Aqueous zinc–iodine batteries are a promising alternative to lithium-ion batteries for stationary energy storage due to their advantages of low cost, environmental friendliness, non-flammability, and easy recyclability. However, their practical application is impeded by the shuttle effect (ShE), which is the migration of triiodide ions from the cathode to the anode and leads to low coulombic efficiency and fast capacity decay. Herein, we investigated the interaction between single atom catalysts (SACs) and iodine species for the selection of appropriate SACs to reduce or obviate the ShE. We found that the desorption of I^- from the SAC surface plays a critical role in maintaining the catalytic activity of SACs to facilitate the iodine reduction reaction. Based on our DFT calculation result, an I^- poisoning mechanism is proposed for SAC selection in Zn−I_2 batteries. A proper SAC should bind I_3^- and facilitate the spontaneous reduction of *I_2 into *I_3 and the subsequent *I desorption from the surface to maintain its activity. In addition, the charge density and partial density of states were determined to understand the interactions between iodine species and SACs. The results showed different charge-transfer and orbital hybridization behaviours. A lower d-band centre can be associated with a more optimal catalytic performance in SACs.

[a] *School of Chemical Engineering and Advanced Materials, The University of Adelaide, Adelaide, SA 5005, Australia. E-mail: shiyong.zhao@adelaide.edu.au, zaiping.guo@adelaide.edu.au*

[b] *Helmholtz Institute Ulm (HIU), Helmholtzstrasse 11, D-89081, Ulm, Germany*

[c] *Shenzhen Geim Graphene Center, Tsinghua-Berkeley Shenzhen Institute & Tsinghua Shenzhen International Graduate School, Tsinghua University, Shenzhen 518055, China*

[d] *Institute for Superconducting and Electronic Materials, School of Mechanical, Materials, Mechatronics and Biomedical Engineering, University of Wollongong, North Wollongong, NSW 2522, Australia*

[e] *School of Science, RMIT University, Melbourne, VIC 3000, Australia*

[f] *Department of Chemistry, Tsinghua University, Beijing 100084, China*

‡ These authors contributed equally to this work.

Introduction

Consumption of dwindling fossil fuels and global climate concerns have initiated vigorous research to explore sources of practical clean and renewable energy.[1][4] Energy conversion techniques such as wind- and solar-generated electricity have been thoroughly explored to maximize energy generation. Because of their intrinsic intermittent nature, however, highly effective energy storage devices are required. Aqueous zinc ion batteries (AZIBs) are a viable alternative to current lithium ion batteries because of their low cost, environmental friendliness, and non-flammability.[5][10] Zinc–iodine ($Zn–I_2$) batteries are attractive because there is an abundance of iodine found in seawater (55 μg per L), and these batteries possess a relatively high theoretical capacity of 211 mA h g^{-1}, with a satisfactory working potential of 1.38 V $vs.$ Zn^{2+}/Zn and resulting energy density.[11][15]

A significant drawback to the practical application of $Zn–I_2$ batteries is the 'shuttle effect' (ShE). Water-soluble triiodide (I_3^-), the intermediate product in the reversible I_2/I^- redox reaction, migrates from the cathode to the anode during repeated charge–discharge, leading to irreversible loss of active mass and significant zinc anode corrosion. The $Zn–I_2$ battery therefore exhibits low coulombic efficiency (CE), fast capacity decay, and limited cycle stability.[16][18] To obviate the ShE, electrolyte re-formulations and separator optimization have been reported. However, for many electrolyte formulations, boosted electrochemical performance is achieved at an economic disadvantage because the solid/quasi-solid and concentrated electrolyte used are more expensive than typical dilute aqueous electrolytes.[19][21] Replacing routine separators of polypropylene and glass fibres with metal organic frameworks or a zeolite membrane separator can prevent the migration of I_3^- from the cathode to the anode, but it will not stop the dissolution of I_3^- from the cathode.[22][24] A drawback of triiodide confinement in porous host materials is that weak physical adsorption cannot suppress the ShE in long-term cycling. It is necessary therefore to suppress the ShE to obtain high-performance $Zn–I_2$ batteries.[24][27]

Single atom catalysts (SACs), in which all of the active metal species exist as isolated single atoms stabilized by support materials, engage in maximum atom utilization compared with bulk metal and nanoparticle catalysts.[28,29] SACs exhibit strong chemical interactions and high catalytic effects in batteries.[30] The adsorption ability and catalytic activity are critical in suppressing the ShE and promoting conversion kinetics in lithium–sulphur batteries.[30][32] It was hypothesized that because of the positive effect of SACs in lithium–sulphur batteries, these would have robust triiodide adsorption capability and fast conversion kinetics to reduce or obviate the ShE in $Zn–I_2$ batteries. Recently, SANi and SAFe were investigated to determine if these catalysts could boost the performance of $Zn–I_2$ batteries.[33,34] However, in these studies, SACs were randomly selected, and the catalytic and adsorption behaviour of different SACs were not investigated. It remains challenging to search for appropriate SACs to suppress the ShE in $Zn–I_2$ batteries because of the current poor understanding of the interaction between SACs and iodine species.

Herein, we report SACs with the ability to boost triiodide conversion and adsorption to suppress the ShE, with resulting high reversible capacity and excellent durability in $Zn–I_2$ batteries. To expedite the search for suitable SACs, we conducted theoretical computations to compare the catalytic performance of eight SACs, namely, SACu, SANi, SACo, SAFe, SAMn, SAV, SAZn, and SATi, and their ability to adsorb triiodide. We found that SACu binds I_3^- and facilitates the spontaneous reduction of *I_2 into *I_3 and the subsequent *I desorption from the surface, with the reduction from *I_3 to *I as the rate-determining step. This allows for reversible and continuous reactions to take place at a comparatively lower overpotential/energy barrier as compared to other SACs.

We also found that due to the strong adsorption of I on the metal active centre, several SACs were inactive and therefore were not efficient in suppressing the ShE. Single atom Cu- and Co-embedded nitrogen-doped Ketjen black (SACu@NKB and SACo@NKB, respectively) were synthesized for performance evaluation. SACu@NKB exhibited superior electrochemical performance in reversible capacity and cycling stability. We showed, via UV-Vis and Raman spectroscopy, and XPS, that SACu@NKB significantly suppressed triiodide shuttling. Experiments confirmed that SACu@NKB boosted the reaction kinetics and possessed the lowest activation energy for iodine reduction. Theoretical computations on charge density and partial density of states (PDOS) were carried out to understand the interactions between iodine species and SACs. The results showed different charge-transfer and orbital hybridization behaviour, in which CoN_4 loses electrons and CuN_4 gains electrons following the adsorption of *I_3. The rate-limiting steps in these redox reactions were identified, and the overpotential was estimated, and these were found to be dependent on the d-band centre of SACs. The lower d-band centre can be associated with a stronger catalytic performance in SACs. We concluded that SACs can be used to suppress the ShE and boost the performance of $Zn–I_2$ batteries. Our findings will be beneficial for designing electrodes in high-performance rechargeable batteries, and therefore will be of wide interest to researchers and manufacturers.

Results and discussion

Understanding triiodide adsorption and conversion on SACs

DFT computations were performed to investigate the electronic properties of various SACs with metal–N_4 structures and their chemical interaction with I_2 and its intermediates. We initially confirmed the interaction between I_2-based species and different sites on SACu, including Cu (as a metal site), C, and N (Fig. 1a). As shown in Fig. 1b, I_2 is in its most thermodynamically favorable state when adsorbed at the Cu site, followed by the N and C sites, accordingly. The free energy diagram in Fig. 1c also shows that the lowest energy barrier for I_2 reduction and oxidation reactions is at the Cu site. The full reduction
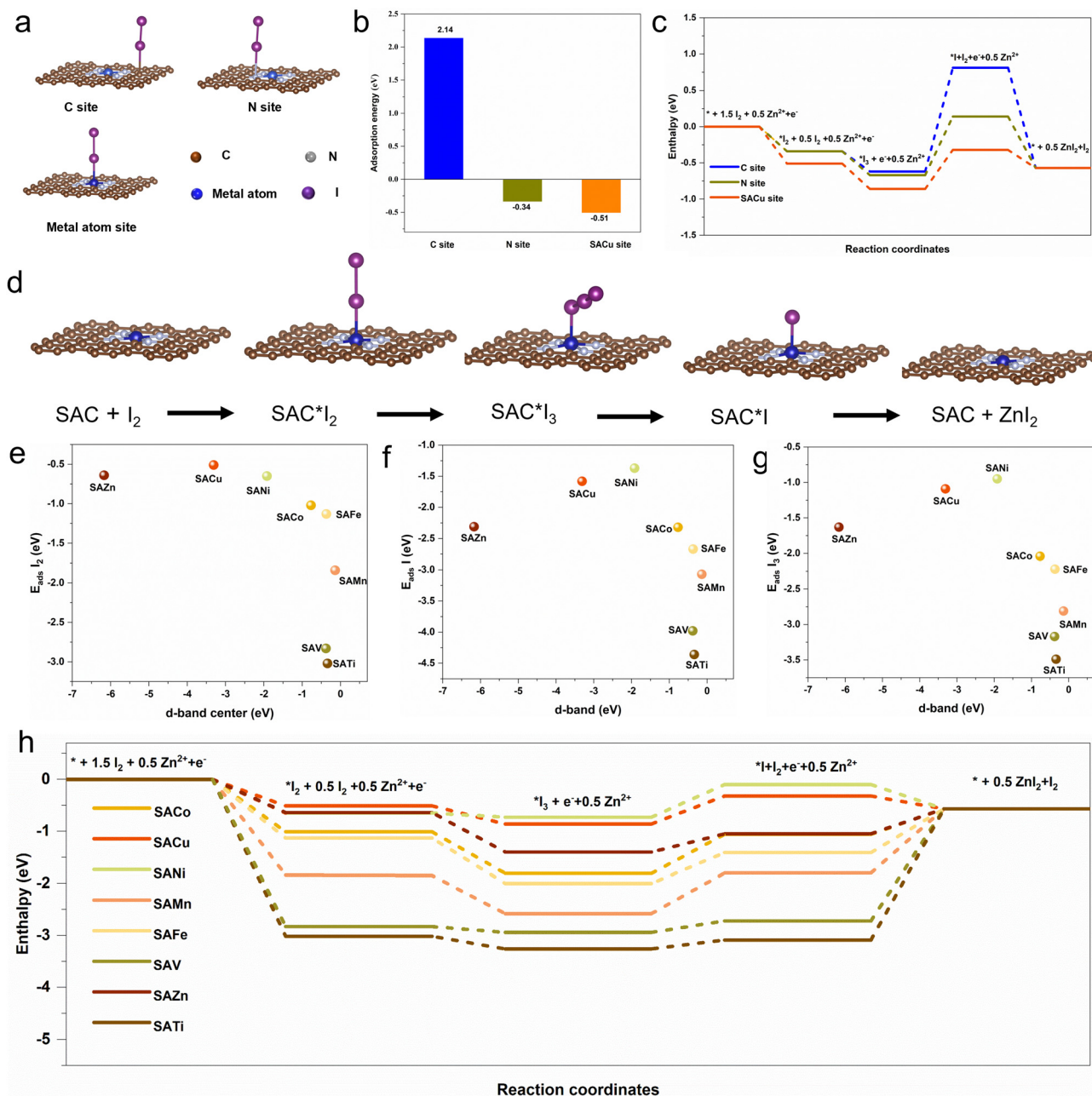
Fig. 1 DFT computations for selected SACs for triiodide adsorption and conversion. (a) Model constructions showing the interaction between three representative active sites in SACs@NG. (b) Adsorption energy for I_2 on C, N, and metal atom sites. (c) Gibbs free-energy diagram for I_2 reduction on C, N, and metal atom sites. (d) Model constructions showing the interaction of I_2 and intermediates with SACs@NG. The relationship between the d-band center of different SACs and the adsorption energies of different species of (e) $*I_2$, (f) $*I$, and (g) $*I_3$. (h) Enthalpy diagram for the I_2 reduction reaction on SACs.

reaction pathway is as follows: $I_2 \rightarrow *I_2 \rightarrow *I_3 \rightarrow *I \rightarrow ZnI_2$, as described in Fig. 1d and Fig. S1 (ESI†). Three intermediates of $*I_2$, $*I_3$, and $*I$ are considered.

The relationship of their adsorption energies and the clean SAC electronic properties of the d-band center is presented in Fig. 1e–g. The volcano plot trend indicates that there are four potential SAC candidates: SAZn, SACu, SANi, and SaCo. These four SACs exhibited interactions with intermediate species at relatively lower adsorption energies, allowing them to facilitate

reversible reactions with greatly facilitated adsorption (bond formation) and desorption (bond breaking). Fig. 1h shows the free energy diagram for I_2 reduction to I on selected SACs.

We found that the iodine reduction reaction (IRR) rate-determining step is different for different SACs. Conversion from $*I_3$ to $*I$ on the surface is the rate-determining step for SACo, SANi, SACu, and SAZn, whereas the desorption of $*I$ from the surface is the IRR rate-determining step for SAMn, SATi, SAFe, and SAV. A lower energy barrier in the rate-determining

step for IRR will provide insights for discovering SACs with lower overpotential. We can also define the rate-determining step for the iodine evolution reaction (IER), which is identical for all SACs investigated herein, and is the desorption of $*I_2$ from the surface.

Mitigation of the ShE for I_3^- is needed to protect the Zn anode, and from our DFT calculations, we understand that the benefits provided by SACs originate from their ability to completely reduce I_2 and its intermediates on the surface to form I^-. We also found that some SACs, such as SATi, SAV, and SAMn, are well-suited for capturing I_3^- on the surface (as shown from their adsorption energies). However, their high energy barrier/overpotential for $*I$ desorption indicates that they may not be ideal candidates for this application. Moreover, this finding also indicates that selection of the metal is critical because it acts as the active center for the I_2 reduction reaction, and also because each metal possesses different electronic properties that can affect the thermodynamics and kinetics of the reaction.[35] The poisoning of the active center due to the strong interaction between intermediates and metal sites is another important factor to be considered to ensure the effectiveness of the SACs in maintaining the reaction.

Maintaining the availability of active sites or the capability to adsorb and desorb intermediates is important for SACs.[36–38] This is best reflected by SACs in the volcano peak. Ideal SACs are those with intermediate adsorption energies, as they allow reversible adsorption, conversion, and desorption on the surface. For this study, we selected SACu (left side of SANi, with a d-band center of −3.31 eV) and SACo (right side of SANi, with a d-band center of −0.77 eV) for further investigation in experiments.

Synthesis and characterization of SACs

Ideally, we do not want the SAC to have a strong or weak affinity toward I_2, I_3^-, or I^- because it will either kill the active sites or be totally non-reactive. Based on findings from theoretical computations, SACu and SACo supported on NKB were synthesized *via* a nitrogen-coordination method (see the ESI†). The synthesis can be readily scaled for production of SAMe@NKB for commercialization, as shown in Fig. S2 (ESI†).

Transmission electron microscopy (TEM) was used to determine the morphology for NKB, SACo@NKB, and SACu@NKB. As presented in Fig. S3 (ESI†), all three samples exhibited the same morphology, confirming that SAC loading did not meaningfully change the morphology of the supporting NKB.

High-angle annular dark-field scanning transmission electron microscopy (HAADF-STEM) images were used to determine the atomic dispersion of single Cu atoms on NKB, as shown in Fig. 2a and b. The resulting HAAD-STEM images confirmed that mono-dispersed single Cu atoms were randomly distributed on the NKB surface, with an average particle size of approximately 0.3 nm, and there were no apparent large-sized Cu particles or clusters. This was further verified in the SACu@NKB XRD pattern, in which no peak associated with Cu metal was observed (Fig. S4, ESI†). The energy dispersive spectroscopy (EDS) elemental mapping confirmed the homogenous distribution of C, N, and Cu elements throughout the structure. The mass loading for SACu on NKB was determined to be 5.4 wt%, *via* inductively coupled plasma-optical emission spectroscopy (ICP-OES).

The atomic structure and coordination state of SACu@NKB was determined *via* synchrotron radiation-based X-ray fine structure spectroscopy (XAFS). The XANES spectra for the Cu K-edge of SACu@NKB was compared with that for Cu foil and Cu_2O, as shown in Fig. 2d. The adsorption edge for SACu@NKB was between Cu foil and Cu_2O, demonstrating that the valence state for Cu in SACu@NKB was between 0 and +1. The extended XAFS, in Fig. 2e, confirmed the coordination state of Cu in SACu@NKB. The Fourier-transformed (FT) k^2-weighted extended XAFS (EXAFS) for Cu in SACu@NKB exhibited a main peak at approximately 1.53 Å that was attributed to Cu–N coordination. Similarly, a peak at approximately 1.44 Å that was associated with Cu–O coordination was observed in the Cu_2O spectra. In contrast, a Cu–Cu coordination signal was detected at a higher position of approximately 2.24 Å for the control Cu foil sample.

The coordination environment for Cu in SACu@NKB was also confirmed in the wavelet-transformed analysis of EXAFS (WT-EXAFS), as shown in Fig. 2g–i, where only one maximum, located at approximately 5 Å, appeared in the WT-EXAFS for SACu@NKB. This indicates that Cu exists as a mononuclear, metal-central species without Cu–Cu coordination, and that Cu exists as single atoms in SACu@NKB, which is a finding consistent with those from FT-EXAFS. EXAF fitting for SACu@NKB was carried out at the Cu-K edge to determine the coordination number (Fig. 2f and Fig. S5, and Table S1, ESI†). As shown in Fig. 2f, the Cu atom was coordinated with four atoms at the first coordination shell. An atomic structure model is presented in the Fig. 2f inset.

Similar measurements and analyses were performed for SACo@NKB samples with SACo content of 5.1 wt% (Fig. S6–S9, ESI†). HAADF-STEM images and EDS elemental mapping confirmed the uniform distribution of mono-dispersed Co single atoms on the NKB. XANES spectra confirmed that the as-synthesized Co single atom valence state was between 0 and +3. FT-EXAFS and WT-EXAFS confirmed that Co single atoms coordinate with N atoms in SACo@NKB, rather than as Co–Co coordination in Co foil and Co–O coordination in Co_2O_3.

Electrochemical assessment of SACs

To establish the effect of SACs on Zn–I_2 redox reactions, the electrochemical performances were assessed of Zn–I_2 batteries with NKB, SACo@NKB, and SACu@NKB cathodes. Fig. 3a presents the cycling performance for Zn–I_2 batteries under a current density of 0.2 A g^{-1}. The NKB cathode without SACs exhibited a relatively low reversible capacity of 121 mA h g^{-1} following 200 cycles, with an average CE of 91.3%.

In contrast, the SACo@NKB and SACu@NKB cathode exhibited greater reversible capacity and CE. A high capacity of 183 mA h g^{-1} and an average CE of 98.4% were exhibited following 200 cycles in the Zn–I_2 battery with SACu@NKB. In accordance with theoretical computations, SACu@NKB outperformed SACo@NKB.
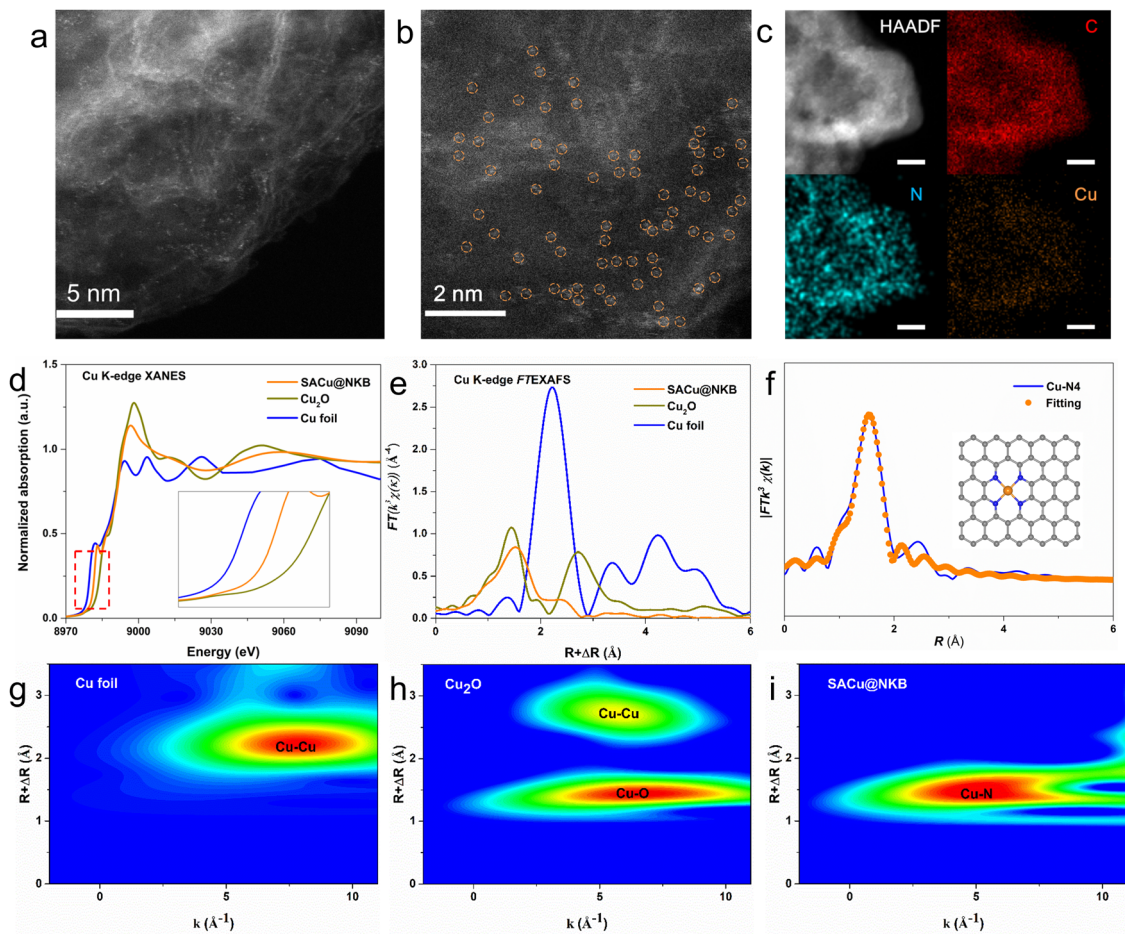
Fig. 2 Structural characterization of SACu@NKB. (a,b) Representative HAADF-STEM images of SACu@NKB. (c) STEM-EDS elemental mapping for SACu@NKB. Scale bar = 5 nm. (d) Normalized Cu K-edge XANES and (e) FT-EXAFS spectra for SACu@NKB, Cu foil, and Cu$_2$O. (f) FT-EXAFS-fitted curves for the Cu-K edge for SACu@NKB. (g)–(i) WT contour plot for the Cu-K edge at the R space for SACu@NKB, Cu foil, and Cu$_2$O.

The superior reaction kinetics for the SACu@NKB and SACo@NKB cathodes were confirmed *via* rate performance measurements under current densities ranging from 0.2 to 8 A g^{-1}. The discharge capacities for the SACu@NKB cathode were 212, 204, 189, 170, 141, and 92 mA h g^{-1} at current densities of 0.2, 0.4, 1, 2, 4, and 8 A g^{-1}, respectively.

These were significantly greater than those for SACo@NKB and NKB. When the current density was set once more to 0.2 A g^{-1}, the SACu@NKB cathode reversible capacity increased to 206 mA h g^{-1}, which demonstrated the high reversibility of the Zn–I$_2$ redox reaction in the electrode. Charge–discharge curves from rate testing indicated the low polarization of Zn–I$_2$ batteries with the SACu@NKB cathode, as shown in Fig. 3c.

The long-term stability was established under a high current density of 2 A g^{-1}. All three cathodes exhibited a similar reversible capacity of approximately 230 mA h g^{-1} at the initial cycle. However, the specific capacity for NKB-based batteries rapidly decreased to approximately 117 mA h g^{-1} following 100 cycles, and the battery failed after approximately 900 cycles (Fig. 3d). The SACu@NKB and SACo@NKB cathodes maintained a greater specific capacity of 165 and 128 mA h g^{-1}, respectively, over 1800 cycles. The SACu employed in this work

was rather stable within the testing voltage window, and the capacity originating from single atoms in combination with the carbon cloth was negligible (Fig. S10, ESI†).

To further investigate the positive impact of SACs on Zn–I$_2$ batteries, SACu@NKB with different amounts of SACu were also tested under a current density of 2 A g^{-1}. As shown in Fig. S11 (ESI†), the 3.2 wt% SACu@NKB cathode exhibited a relatively low capacity of 137 mA h g^{-1} after 1800 cycles. In contrast, the 5.4 wt% and 8.5 wt% SACu@NKB cathodes delivered a similar specific capacity of 170 mA h g^{-1} over 1800 cycles, indicating that an SACu loading of 5.4 wt% was sufficient to boost the performance of the Zn–I$_2$ batteries. The significant cycling stability of the as-synthesized SACu@NKB and SACo@NKB cathodes was also exhibited at a greater current density of 5 A g^{-1}. Fig. 3f (and Fig. S12, ESI†) demonstrate that the Zn–I$_2$ battery with a SACu@NKB cathode exhibited a specific capacity of 121 mA h g^{-1} following the initial 20 cycles, and maintained capacity at 112 mA h g^{-1} following 5000 cycles, with a capacity retention of 92.5%. Compared with other studies, these findings show cycling stability and reversible capacity that is comparable to that of previously reported representative Zn–I$_2$ batteries, as shown in Fig. 3e.[16,18,22,23,25,39–42]
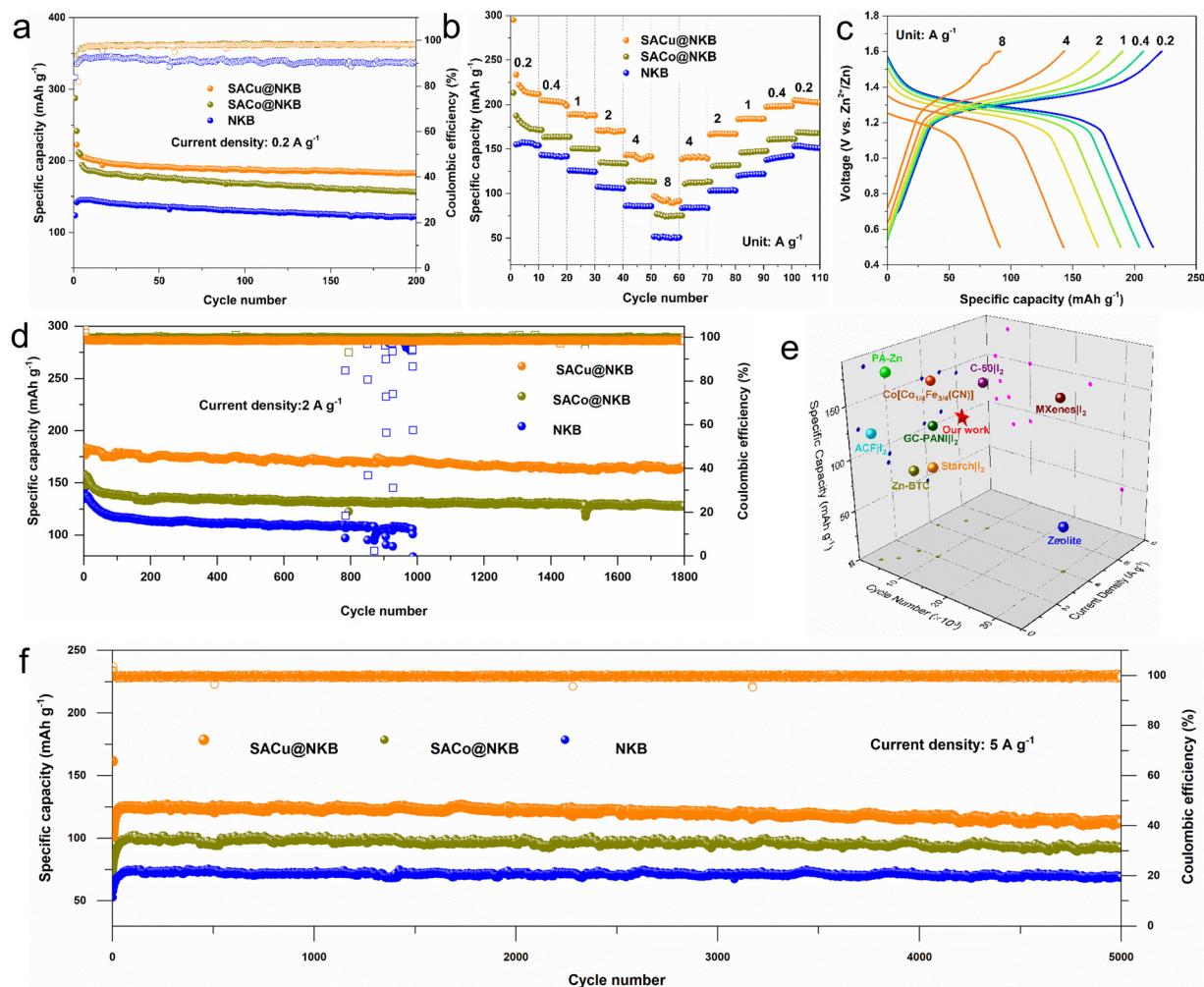
Fig. 3 Electrochemical performance for the Zn–I_2 battery with NKB, SACo@NKB, and SACu@NKB cathodes. (a) Cycling stability and Coulombic efficiency at 0.2 A g^{-1}. (b) Rate performance at current densities from 0.2 to 8 A g^{-1}, and (c) corresponding charge–discharge profiles at differing current densities. (d) Cycling stability for Zn–I_2 batteries at 2 A g^{-1}. (e) Comparison between Zn–I_2 batteries with the SACu@NKB cathode and reported values. (f) Long-term cycling stability under a high current density of 5 A g^{-1}.

Shuttle effect (ShE)

SACs strongly interact with the triiodine ion, and this contributes to the suppression of ShE when SAC cathodes are used in Zn–I_2 batteries. As shown in Fig. 4a, following the addition of an identical amount of NKB and SACu@NKB in the triiodide solution, the original yellow-coloured triiodide solution remained coloured after the addition of NKB. In contrast, the solution exposed to SACu@NKB powder became nearly transparent, which indicated greater adsorption ability of SACs compared with porous-carbon NKB (Fig. 4a).

The high bonding strength of SACs is important for the prevention of re-dissolution of triiodide during battery cycling. To compare the strength of the bonds between NKB and triiodide and SACu@NKB and triiodide, NKB/triiodide and a SACu@NKB/triiodide mixture were harvested from solution and immersed in deionized (DI) water. As presented in Fig. S13 (ESI†), re-dissolution of triiodide was found in NKB/triiodide, which resulted in the transparent DI water becoming

a light yellow colour, whilst the DI water remained transparent following the addition of the SACu@NKB/triiodide mixture, thus confirming that triiodide re-dissolution was obviated. From the SEM image and corresponding EDS elemental mapping findings (Fig. S14, ESI†), no triiodide particles or clusters were observed, and the triiodide was homogenously distributed on the SACu@NKB support.

The capacity of SACs to adsorb triiodine was confirmed *via* UV-Vis spectra (Fig. 4b). Strong peaks with maximum adsorption wavelength located at 288 and 350 nm are associated with triiodide.[43] The ability of SACu@NKB to adsorb triiodide solution was superior because when triiodide solution was exposed to SACu@NKB powder, there was weaker absorbance compared with SACo@NKB and NKB. To quantify the specific triiodide adsorption capacity of the as-prepared NKB, SACo@NKB, and SACu@NKB, the relationship between concentration and absorbance was determined *via* assessing the standard triiodide solution, as shown in Fig. S15 (ESI†). By applying the
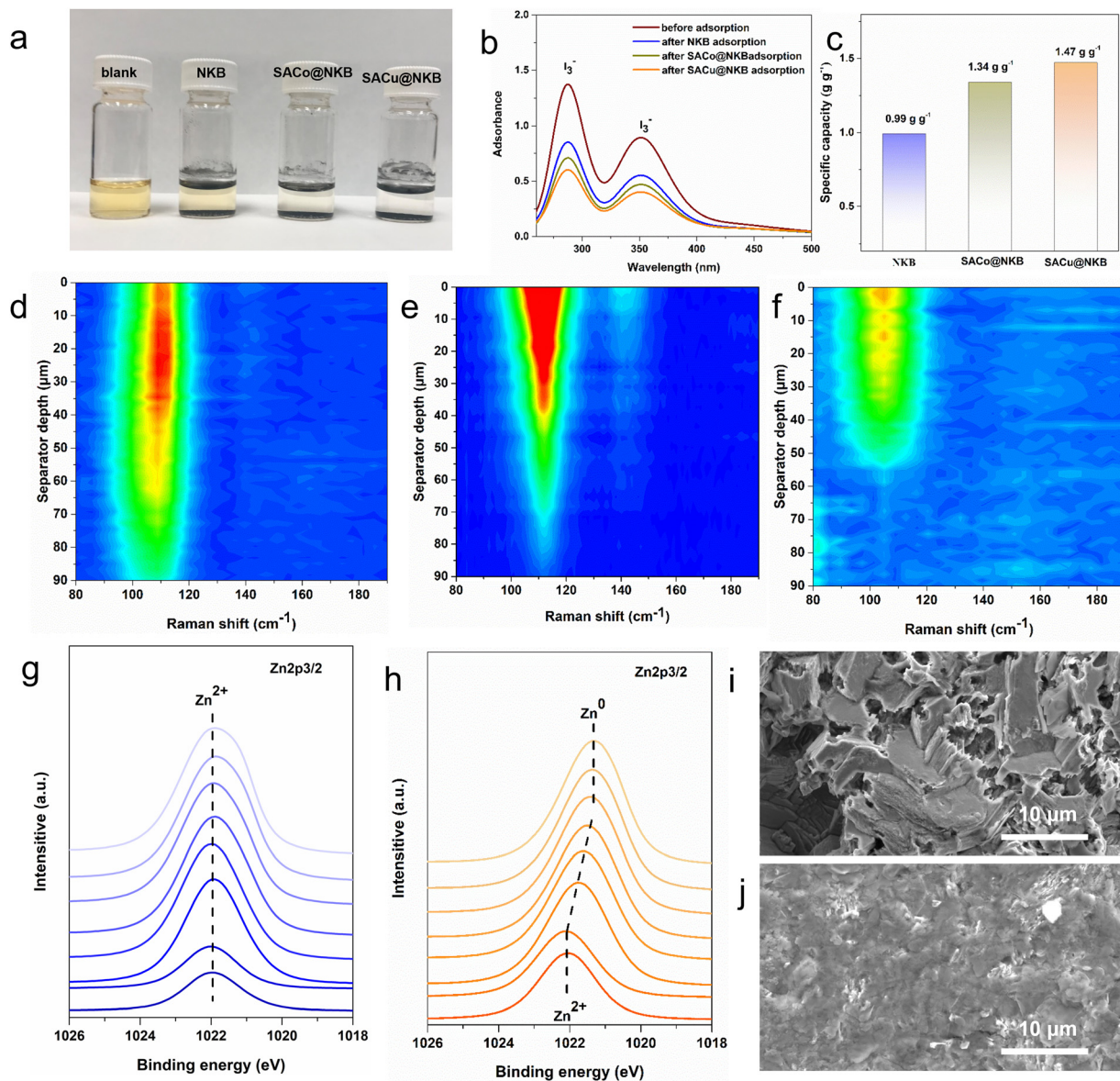
Fig. 4 Suppression of the shuttle effect in Zn–I$_2$ batteries with SAC@NKB cathodes. (a) Photographs showing triiodide capture by NKB, SACo@NKB, and SACu@NKB. (b) UV-Vis spectra of triiodide solutions prior to and following capture in NKB, SACO@NKB, and SACu@NKB, and (c) corresponding triiodide species capture capacities. Raman line-scan on aqueous filter membrane separator cross-section from cathode-side to anode-side following the first cycle for the (d) NKB, (e) SACo@NKB, and (f) SACu@NKB cathodes. Zn 2p$_{3/2}$ XPS depth profiles for Zn anodes following 50 cycles in the Zn–I$_2$ battery with (g) NKB and (h) SACu@NKB cathodes. SEM images of the Zn anode following 50 cycles in the (i) NKB-based Zn–I$_2$ battery and (j) SACu@NKB-based Zn–I$_2$ battery.

linearity between the UV-Vis absorbance and triiodide concentration, the specific adsorption capacities of NKB, SACo@NKB, and SACu@NKB for triiodide were found to be 0.99, 1.34, and 1.47 g g^{-1}, respectively, as shown in Fig. 4c.

SEM and Raman measurements on the cross-section of the separators following the first cycle were used to establish triiodide shuttling. Fig. S16a (ESI†) shows that the thickness of the aqueous filter membrane separator was approximately 90 μm. EDS elemental mapping analyses from the separator, coupled with the NKB cathode, showed that the I element, which was attributed to triiodide, was mainly distributed on the upper side of the separator, attached to the cathode, and the I

signal became weaker as the depth increased. This finding was attributed to the fact that the migration of triiodide ions initially occurred at the cathode. There was a similar finding for the SACu@NKB cathode-based separator, as shown in Fig. S16b (ESI†).

To determine the ShE with different cathodes, a Raman line scan was performed on the cross-section of the separators.[44] For the NKB cathode, the triiodide penetrated through the separator following the first cycle, underscoring the high significance of the ShE because of the relatively weak ability of NKB to adsorb triiodide. Because of the triiodide adsorption ability and excellent catalytic activity of SACs, suppressed

triiodide shuttling was confirmed in batteries coupled with SACo@NKB and SACu@NKB cathodes, as shown in Fig. 4e and f. Importantly, no triiodide signal was detected beyond a 55 μm depth of the separator cross-section with the SACu@NKB cathode.

The shuttling of triiodide negatively impacted the Zn anode.[22] The chemical reaction between triiodide and metallic Zn deteriorated the Zn anode, and the accumulation of insulated byproducts increased dendrite growth, leading to low CE and limited cycling stability. To confirm this, zinc foils were immersed in anolyte with or without triiodide. Following one week of resting, the originally yellow-coloured anolyte solution with triiodide addition became clear, as shown in Fig. S17 (ESI†), which indicated that triiodide was exhausted by parasitic reactions between triiodide and zinc metal.

The zinc metal was collected for additional SEM and XRD measurement. Loose and large particles were observed on the Zn metal immersed in the anolyte with triiodide additive, whereas the Zn metal collected from bare anolyte exhibited an ultra-flat and compact morphology (Fig. S18, ESI†). Additional XRD measurements on the Zn metals confirmed that following immersion of the anolyte with triiodide additive, the large particles on the Zn metal were attributed to the $Zn_4SO_4(OH)_6 \cdot xH_2O$ byproduct (Fig. S19, ESI†).

SEM and XRD measurements carried out on Zn metal following immersion with and without triiodide confirmed that the chemical reaction between triiodide and Zn metal accelerates parasitic Zn corrosion. The Zn electrodes were stripped from the NKB- and SACu@NKB-based Zn–I_2 batteries following cycling and were subjected to XPS, SEM, and XRD measurement. For the NKB cathode, the cycled Zn anode featured a thick passivation layer consisting of $Zn_4SO_4(OH)_6 \cdot xH_2O$ byproduct. In Fig. 4g, there is no metallic Zn (Zn^0) peak in the XPS etching or the SEM image. However, Fig. 4i shows a rough surface with large particles, confirming highly significant Zn corrosion in NKB cathode-based batteries. In contrast, when coupled with the SACu@NKB cathode, as is shown in the XPS depth profile of Fig. 4h, the cycled Zn electrode binding energy shifted from Zn^{2+} to Zn^0 as the etching depth increased. Similar results were also observed for the S 2p XPS spectrum in Fig. S20 (ESI†). The SEM image in Fig. 4j shows a relatively smooth surface, and the XRD pattern (Fig. S21, ESI†) underscores a weaker $Zn_4SO_4(OH)_6 \cdot xH_2O$ byproduct intensity compared with that for the NKB cathode. Therefore, based on the measurements of the cycled Zn electrode, the ShE was significantly suppressed using the SAC cathode, and as a result, the triiodide corrosion and parasitic reactions on the Zn anode were inhibited.

SAC catalytic performance

The electrocatalytic I_2 reduction performance of SACs was determined using cyclic voltammetry (CV) measurements. Fig. 5a presents the CV curves for the NKB, SACo@NKB, and SACu@NKB cathodes, in which the SACu@NKB cathode exhibited the greatest peak reduction current, followed by the SACo@NKB and NKB cathodes. This finding provides evidence of the superior IRR in the SACu@NKB cathode. Additionally,

SACu@NKB exhibited the greatest cathodic and least anodic voltage, as shown in Fig. S22 (ESI†), with the lowest electrochemical polarization of 89 mV amongst the three cathodes. The lowest electrochemical polarization for SACu@NKB was confirmed in the charge–discharge profile of Fig. S23 (ESI†). The Tafel slope (η), an important indicator for reaction kinetics and catalytic activity, was computed from the CV curves.[45] In Fig. 5b, SACu@NKB exhibited the lowest η of 189 mV dec^{-1}, compared with 201 and 251 mV dec^{-1} for SACo@NKB and NKB, respectively. This relatively low η value indicates the fast reaction kinetics of the SACu@NKB cathode.

The boosted electrocatalytic activity and kinetics of SACu@NKB for the IRR was confirmed via electrochemical impedance spectroscopy (EIS) measurement performed at the reduction onset potential. Charge transfer is important in the ions and electrons migrating to the active central locations for the IRR reaction, and therefore determines the electrocatalytic kinetics.[46] EIS curves showed that the lowest charge transfer resistance was for SACu@NKB, and thus demonstrated the superior charge transfer kinetics (Fig. S24a, ESI†). The charge transfer resistance was measured over a range of temperatures to determine the activation energy (E_a) via the Arrhenius equation:

$$\frac{1}{R_{ct}} = A \exp\left(-\frac{E_a}{R_0 T}\right) \qquad (1)$$

where R_{ct} denotes the charge transfer resistance (Fig. S24b, ESI†). It was determined that the E_a values for SACu@NKB, SACu@NKB, and NKB were 7.382, 8.413, and 9.369 kJ mol^{-1}, respectively (Fig. 5c). The lowest E_a was consistent with the superior kinetics for SACu@NKB to participate in the electrocatalytic IRR.

To determine how the SACs boost the electrocatalytic kinetics, theoretical computations on charge density and partial density of states (PDOS) were carried out to understand the ShE in SACo and SACu following their interaction with I_3^-. The charge density for SACo*I_3 and SACu*I_3 are presented in Fig. 5d and e (and Fig. S25, ESI†). Bader charge analysis was used to determine the charge distribution. The SACo and SACu substrates exhibited a net charge migration of 0.42 $|e|$ and 0.52 $|e|$ to the *I_3. This suggests that following the adsorption of *I_3, CoN_4 loses electrons and CuN_4 gains electrons.

From the PDOS for SACo*I_3, Fig. 5f shows that one of the in-plane Co 3d orbitals, d_{xy}, was empty, as was recognized from the significantly sharp peaks in the spin-up and spin-down. There was no hybridization with I 5p orbitals. The out-plane Co 3d orbital for d_{z^2} was partially filled and exhibited hybridization with I 5p orbitals. The other Co 3d orbitals, d_{xz}, d_{yz}, and d_{x^2}, were full in spin-up and spin-down, and exhibited excellent hybridization with the I 5p orbital. From the PDOS for SACu*I_3, Fig. 5g shows that all Cu 3d orbitals were filled, except for the in-plane, d_{xy}, which was partially filled. Hybridization was observed only between the out-plane Cu 3d orbital of d_{z^2} and I 5p orbitals. Overall, it is understood that SACu has a lower d-band center than that of SACo. In addition, the DFT-calculated bandgaps for pristine SACo and SACu were 0.72
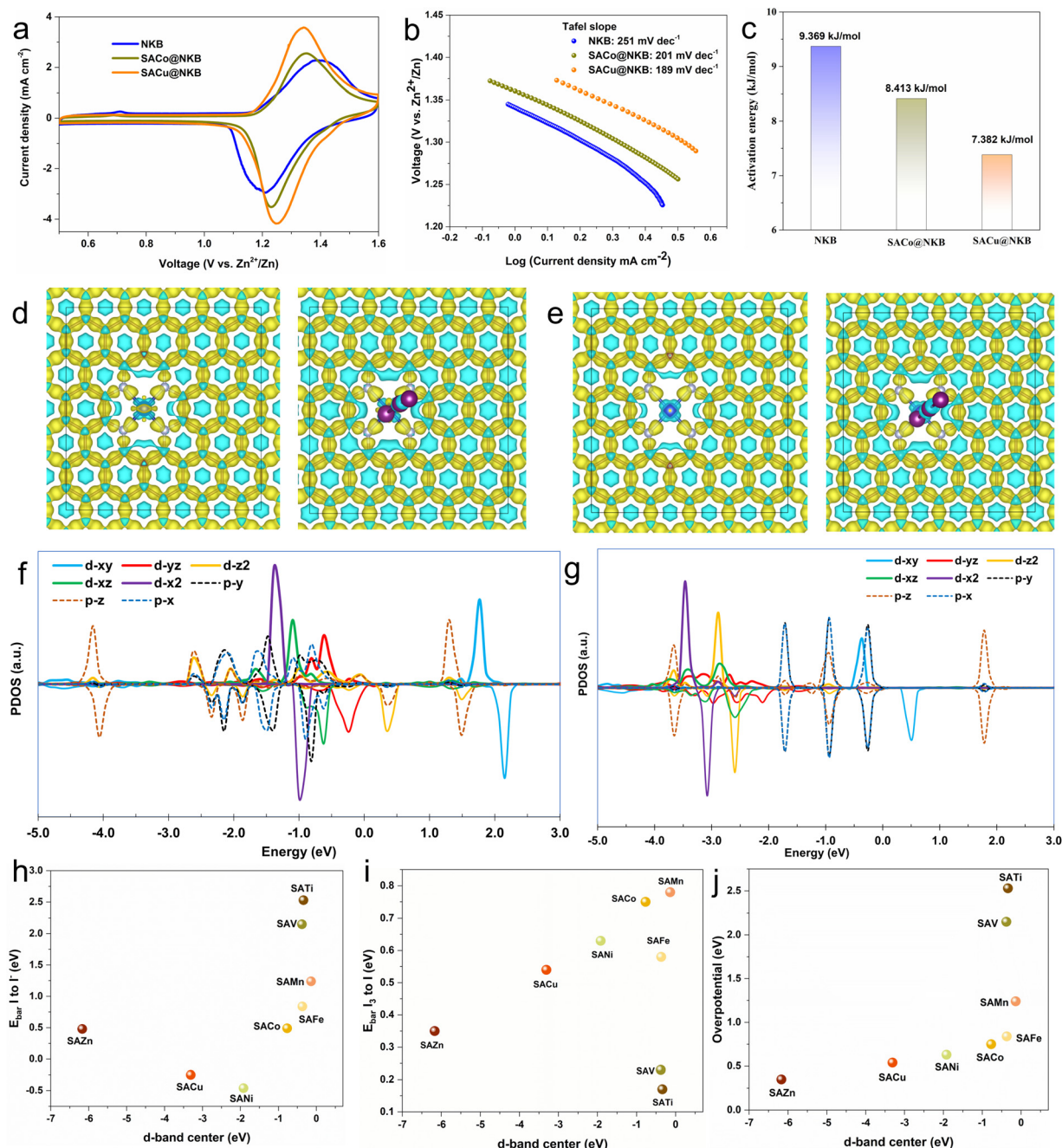
Fig. 5 Catalysis performance for the NKB, SACo@NKB, and SACu@NKB cathodes. (a) CV curves for Zn−I$_2$ batteries, and the corresponding (b) Tafel plot. (c) Comparison of the activation energy for the NKB, SACo@NKB, and SACu@NKB cathodes. (d) SACo and (e) SACu prior to and following adsorption of I$_3^-$. Partial density of states (PDOS) and hybridization between the 5p orbital of I and 3d orbital of (f) Co and (g) Cu, following adsorption of I$_3^-$. Energy barrier for (h) *I to I$^-$ and (i) *I$_3$ to *I reactions on selected SACs. (j) Overpotential as obtained from the energy barrier of the rate-determining step of the I$_2$ reduction reaction on SACs.

and 0.65, eV, respectively. The adsorption of *I$_3$ resulted in bandgaps that decreased to 0.43 and 0.45 eV for SACo and SACu, respectively, indicating the increase in conductivity in the SACs.

As previously described in Fig. 1e–g, a higher d-band center, which is closer to the Fermi level, is equivalent to stronger interactions with I$_2$ and intermediates. However, there are two critical reactions for the IRR pathway that must be considered:

(i) triiodide conversion and (ii) iodine desorption from SACs. The theoretical computations in Fig. 5h and i revealed a correlation between these two reactions with the d-band center of clean SACs. Further analysis of the IRR rate-determining step provided information on the overpotential, as presented in Fig. 5j, which shows trends similar to those in Fig. 5c, where SACu exhibits a lower overpotential than that of SACo for the IRR.

Our experiments demonstrate the superior capability of SACu over SACo, and its key profile originates from its capability to release I⁻ from the surface, thus allowing faster conversion kinetics while at the same time suppressing the ShE of I_3^- in the Zn–I_2 battery. Furthermore, from Fig. 5j, SAZn seems to be a promising SAC candidate because it exhibits the lowest overpotential as compared to the other investigated SACs, even though it exhibits strong adsorption of I_2 intermediates. The investigation of its performance is, however, beyond the scope of this study.

Conclusion

We confirmed that single atom catalysts (SACs) for triiodide (I_3^-) adsorption and conversion suppressed I_3^- shuttling in Zn–I_2 batteries based on the combination of experimentation and computation. The selection of the metal active centre in SACs is important for two reasons: (i) catalytic activity – conversion thermodynamics and kinetics for the I_2/I^- redox reaction, and (ii) reversibility – the active centre remains active or is poisoned following the interaction with different I_2 species. SACu was selected *via* theoretical computation from eight SACs (SACu, SACo, SANi, SAFe, SAMn, SAV, SAZn, and SATi) for its strongest performance of satisfactory catalytic activity and sensible interaction with different I_2 species.

Synthesized SACu@NKB, SACo@NKB, and NKB cathodes were subjected to electrochemical performance testing, and the results indicated that SACu@NKB outperformed SACo@NKB and NKB. Significantly boosted battery reversible capacity, kinetics, and cycle life were confirmed to originate from significant I_3^- adsorption and rapid conversion kinetics with SACu. Our method can be used to effectively obviate I_3^- shuttling and maximize I species utilization, and it can also be applied to electrode design for high-performance rechargeable batteries.

Conflicts of interest

The authors declare no conflicts of interest.

Acknowledgements

References

1 D. Chao and S.-Z. Qiao, *Joule*, 2020, **4**, 1846.
2 B. Dunn, H. Kamath and J.-M. Tarascon, *Science*, 2011, **334**, 928.
3 M. Armand, *Nature*, 2001, **414**, 359.
4 F. Yang, J. Hao, J. Long, S. Liu, T. Zheng, W. Lie, J. Chen and Z. Guo, *Adv. Energy Mater.*, 2021, **11**, 2003346.
5 F. Yang, J. A. Yuwono, J. Hao, J. Long, L. Yuan, Y. Wang, S. Liu, Y. Fan, S. Zhao, K. Davey and Z. Guo, *Adv. Mater.*, 2022, 2206754.
6 Y. Wang, Z. Wang, F. Yang, S. Liu, S. Zhang, J. Mao and Z. Guo, *Small*, 2022, **2107033**, 2107033.
7 B. Tang, L. Shan, S. Liang and J. Zhou, *Energy Environ. Sci.*, 2019, **12**, 3288.
8 J. Hao, L. Yuan, Y. Zhu, M. Jaroniec and S. Z. Qiao, *Adv. Mater.*, 2022, 34, DOI: **10.1002/adma.202206963**.
9 Y. Zhang, X. Zheng, K. Wu, Y. Zhang, G. Xu, M. Wu, H.-K. Liu, S.-X. Dou and C. Wu, *Nano Lett.*, 2022, **22**, 8574.
10 L. Yuan, J. Hao, B. Johannessen, C. Ye, F. Yang, C. Wu, S.-X. Dou, H.-K. Liu and S.-Z. Qiao, *eScience*, 2023, 100096.
11 K. K. Turekian, N. Haven, K. Hans and W. M. Der Universitat, *Geol. Soc. Am. Bull.*, 1961, **72**, 175.
12 P. H. Svensson and L. Kloo, *Chem. Rev.*, 2003, **103**, 1649.
13 B. Li, Z. Nie, M. Vijayakumar, G. Li, J. Liu, V. Sprenkle and W. Wang, *Nat. Commun.*, 2015, **6**, 6303.
14 Y. Zou, T. Liu, Q. Du, Y. Li, H. Yi, X. Zhou, Z. Li, L. Gao, L. Zhang and X. Liang, *Nat. Commun.*, 2021, **12**, 170.
15 J. Hao, L. Yuan, B. Johannessen, Y. Zhu, Y. Jiao, C. Ye, F. Xie and S. Qiao, *Angew. Chem.*, 2021, **133**, 25318.
16 L. Ma, Y. Ying, S. Chen, Z. Huang, X. Li, H. Huang and C. Zhi, *Angew. Chem., Int. Ed.*, 2021, **60**, 3791.
17 E. Gwynne, B. H. Davies and E. Gwynne, *J. Am. Chem. Soc.*, 1952, **74**, 2748.
18 S. Zhang, J. Hao, H. Li, P. Zhang, Z. Yin, Y. Li, B. Zhang, Z. Lin and S. Qiao, *Adv. Mater.*, 2022, **34**, 2201716.
19 Y. Yang, S. Liang, B. Lu and J. Zhou, *Energy Environ. Sci.*, 2022, **15**, 1192.
20 H. K. Machhi, K. K. Sonigara, S. N. Bariya, H. P. Soni and S. S. Soni, *ACS Appl. Mater. Interfaces*, 2021, **13**, 21426.
21 J. J. Hong, L. Zhu, C. Chen, L. Tang, H. Jiang, B. Jin, T. C. Gallagher, Q. Guo, C. Fang and X. Ji, *Angew. Chem.*, 2019, **131**, 16057.
22 Z. Li, X. Wu, X. Yu, S. Zhou, Y. Qiao, H. Zhou and S.-G. Sun, *Nano Lett.*, 2022, **22**, 2538.
23 H. Yang, Y. Qiao, Z. Chang, H. Deng, P. He and H. Zhou, *Adv. Mater.*, 2020, **32**, 2004240.
24 C. Xie, Y. Liu, W. Lu, H. Zhang and X. Li, *Energy Environ. Sci.*, 2019, **12**, 1834.
25 X. Li, N. Li, Z. Huang, Z. Chen, G. Liang, Q. Yang, M. Li, Y. Zhao, L. Ma, B. Dong, Q. Huang, J. Fan and C. Zhi, *Adv. Mater.*, 2021, **33**, 2006897.
26 H. Park, R. K. Bera and R. Ryoo, *Adv. Energy Sustainability Res.*, 2021, **2**, 2100076.
27 C. Bai, F. Cai, L. Wang, S. Guo, X. Liu and Z. Yuan, *Nano Res.*, 2018, **11**, 3548.

28 Z. H. Xue, D. Luan, H. Zhang and X. W. (David) Lou, *Joule*, 2022, **6**, 92.

29 R. Li and D. Wang, *Adv. Energy Mater.*, 2022, **12**, 1.

30 C. Lu, R. Fang and X. Chen, *Adv. Mater.*, 2020, **32**, 1906548.

31 Y. Liu, Z. Wei, B. Zhong, H. Wang, L. Xia, T. Zhang, X. Duan, D. Jia, Y. Zhou and X. Huang, *Energy Storage Mater.*, 2021, **35**, 12.

32 Y. Li, S. Lin, D. Wang, T. Gao, J. Song, P. Zhou, Z. Xu, Z. Yang, N. Xiao and S. Guo, *Adv. Mater.*, 2020, **32**, 1.

33 X. Yang, H. Fan, F. Hu, S. Chen, K. Yan and L. Ma, *Nano-Micro Lett.*, 2023, **15**, 1.

34 L. Ma, G. Zhu, Z. Wang, A. Zhu, K. Wu, B. Peng, J. Xu, D. Wang and Z. Jin, *Nano Lett.*, 2023, **23**, 5272.

35 Q. Qu, S. Ji, Y. Chen, D. Wang and Y. Li, *Trends Chem.*, 2021, **3**, 954.

36 D. Chakraborty, T. E. L. Smitshuysen, A. Kakekhani, S. P. F. Jespersen, S. Banerjee, A. Krabbe, N. Hagen, H. Silva, J. Just, C. D. Damsgaard, S. Helveg, A. M. Rappe, J. K. Nørskov and I. Chorkendorff, *J. Phys. Chem. C*, 2022, **126**, 16194.

37 J. A. Yuwono, N. Birbilis, R. Liu, Q. Ou, Q. Bao and N. V. Medhekar, *J. Electrochem. Soc.*, 2017, **164**, C918.

38 J. A. Yuwono, N. Birbilis, C. D. Taylor, K. S. Williams, A. J. Samin and N. V. Medhekar, *Corros. Sci.*, 2019, **147**, 53.

39 L. Zhang, M. Zhang, H. Guo, Z. Tian, L. Ge, G. He, J. Huang, J. Wang, T. Liu, I. P. Parkin and F. Lai, *Adv. Sci.*, 2022, **9**, 2105598.

40 W. Li, K. Wang and K. Jiang, *J. Mater. Chem. A*, 2020, **8**, 3785.

41 S. Chen, Q. Chen, J. Ma, J. Wang, K. S. Hui and J. Zhang, *Small*, 2022, **18**, 2200168.

42 H. Pan, B. Li, D. Mei, Z. Nie, Y. Shao, G. Li, X. S. Li, K. S. Han, K. T. Mueller, V. Sprenkle and J. Liu, *ACS Energy Lett.*, 2017, **2**, 2674.

43 J. L. Pursell and C. J. Pursell, *J. Phys. Chem. A*, 2016, **120**, 2144.

44 M. Savastano, C. Bazzicalupi, C. García, C. Gellini, M. D. López de la Torre, P. Mariani, F. Pichierri, A. Bianchi and M. Melguizo, *Dalton Trans.*, 2017, **46**, 4518.

45 X. Zheng, J. Yang, Z. Xu, Q. Wang, J. Wu, E. Zhang, S. Dou, W. Sun, D. Wang and Y. Li, *Angew. Chem., Int. Ed.*, 2022, 61, DOI: **10.1002/anie.202205946.**

46 L. Peng, Z. Wei, C. Wan, J. Li, Z. Chen, D. Zhu, D. Baumann, H. Liu, C. S. Allen, X. Xu, A. I. Kirkland, I. Shakir, Z. Almutairi, S. Tolbert, B. Dunn, Y. Huang, P. Sautet and X. Duan, *Nat. Catal.*, 2020, **3**, 762.